Effect of ionic disorder on the principal shock Hugoniot

Crystal F. Ottoway, Daniel A. Rehn ⬤, Didier Saumon ⬤, and C. E. Starrett[*]

Los Alamos National Laboratory, P.O. Box 1663, Los Alamos, New Mexico 87545, USA

The effect of ionic disorder on the principal Hugoniot is investigated using multiple scattering theory to very high pressure (Gbar). Calculations using molecular dynamics to simulate ionic disorder are compared to those with a fixed crystal lattice, for both carbon and aluminum. For the range of conditions considered here we find that ionic disorder has a relatively minor influence. It is most important at the onset of shell ionization and we find that, at higher pressures, the subtle effect of the ionic environment is overwhelmed by the larger number of ionized electrons with higher thermal energies.

I. INTRODUCTION

The principal shock Hugoniot is the locus of final states in single-shock experiments where the material is initially at standard temperature and pressure. It is a method with a long history [1] and it is used to measure the equation of state at high pressures and temperatures. In flyer plate shock experiments, a pusher is driven into the material of interest, launching a shock wave. In laser-driven shock experiments, a layer of ablator material is laser heated. The rapid expansion of the ablator launches a shock wave into the target material. Conservation of mass, energy, and momentum across the shock front and the assumption of an ideal shock translate the measured pusher and shock front velocities into the desired equation of state variables.

Recent experiments at the National Ignition Facility (NIF) [2] have resulted in accurate measurements of the Hugoniot curve at very high pressures [3] and are of relevance to inertial confinement fusion and white dwarf physics [4]. These experiments at hundreds of Mbar complement the older, lower-pressure techniques, including gas-gun technology [5], diamond anvil cells [6], and lower-energy laser compression [7,8], that have challenged and guided equation of state (EOS) models and tables for many years [9].

Models for the equation of state have for many years used these experiments for validation and testing. Practical models, used to build equation of state tables, need to be reasonably accurate, computationally cheap, and applicable over a huge range of conditions and materials. These pragmatic restrictions often require the use of simplified models of the EOS physics. For example, many widely used EOS tables are based on so-called average atom models. These attempt to capture the properties of one averaged atom that is representative of the system [10–15], but do not include the effect of ionic disorder. As a result, ionic disorder has to be included via a separate model [16–18].

The effect that a consistent treatment of ionic disorder has on Hugoniot curves remains largely untested for dense plasmas. Some modeling methods are capable of evaluating this.

For example, the widely used density functional theory (DFT) molecular dynamics (MD) method includes ionic disorder through the use of ensemble averaging over MD time steps [19,20]. While accurate, this method is generally limited to degenerate systems (read lower temperature, higher density) due to computational expense and contains the additional complication of pseudopotentials. Several recent works have presented solutions to the problem of temperature scaling of the computational expense of DFT MD [21–26]. Another method that includes ionic disorder is path integral Monte Carlo [27]. This is also an accurate method, but is generally restricted to high temperatures due to the fermion sign problem [27].

Recently, a DFT-based method that can reach high temperatures and that does not use pseudopotentials has been developed. This method, known as multiple scattering theory (MST), has a long history in solid state physics [28,29]. It has recently been adapted to high-temperature dense plasmas [30,31]. Multiple scattering theory includes a sophisticated DFT treatment of the electrons and includes ionic disorder through ensemble averaging over ionic configurations obtained with molecular-dynamics simulations.

In this work, we use MST to assess the impact of ionic disorder on the principal Hugoniots of carbon and aluminum. We report results up to several Gbar using both ionic configurations from molecular dynamics and a fixed crystal lattice structure. We also compare our results to those from an average atom model and existing *ab initio* simulations [27]. We find that inclusion of ionic disorder has a relatively small effect on the Hugoniot, but this effect is larger for aluminum than carbon. Further, we find that at high pressures, where the plasma is significantly ionized, a crude treatment of ionic disorder is accurate enough for Hugoniot predictions.

II. METHOD

The methods used here are described in detail in Refs. [30,31]. In this section, we give a broad summary, sufficient to allow the reader to assess the results presented and get a broad understanding of the method itself, together

*starrett@lanl.gov

055208-1

with calculational details. If more detail is desired, we refer the reader to Refs. [30,31].

Multiple scattering theory is based on the idea that the time-independent Green's function for a system containing electrons and nuclei can be found by solving Dyson's equation. This equation relates the *a priori* unknown Green's function $G(\boldsymbol{x}, \boldsymbol{x}', \epsilon)$ to the known Green's function of some reference system $g(\boldsymbol{x}, \boldsymbol{x}', \epsilon)$ [32],

$$G(\boldsymbol{x}, \boldsymbol{x}', \epsilon)$$
$$= g(\boldsymbol{x}, \boldsymbol{x}', \epsilon) + \int d\boldsymbol{x}_1 G(\boldsymbol{x}, \boldsymbol{x}_1, \epsilon) V(\boldsymbol{x}_1) g(\boldsymbol{x}_1, \boldsymbol{x}', \epsilon), \quad (1)$$

where $V(\boldsymbol{x})$ is the potential difference between the reference system and the desired electron-nucleus system. Choosing a free-electron reference system,

$$g(\boldsymbol{x}, \boldsymbol{x}', \epsilon) = -\frac{m_e}{2\pi} \frac{\exp(\iota|\boldsymbol{x} - \boldsymbol{x}'|)}{|\boldsymbol{x} - \boldsymbol{x}'|}, \quad (2)$$

where m_e is the electron mass and $V(\boldsymbol{x})$ becomes the potential for the electron-nucleus system.

The next step is to carry out a multicenter expansion of the Green's functions using spherical harmonics $Y_{lm}(\hat{\boldsymbol{r}})$. The positions of the expansion centers were originally chosen to coincide with the nuclear positions [28,29]. This works well for close-packed crystal structures. However, it is not appropriate for disordered plasmas, and in addition to these nuclear centers, extra expansion centers are used [30]. These expansion centers are used to tessellate space into space-filling, nonoverlapping cells. The result of this multicenter expansion is

$$G(\boldsymbol{r} + \boldsymbol{R}^n, \boldsymbol{r}' + \boldsymbol{R}^{n'}, z) = G^{ss}(\boldsymbol{r} + \boldsymbol{R}^n, \boldsymbol{r}' + \boldsymbol{R}^{n'}, z)$$
$$+ G^{ms}(\boldsymbol{r} + \boldsymbol{R}^n, \boldsymbol{r}' + \boldsymbol{R}^{n'}, z), \quad (3)$$

where $\boldsymbol{R}^n$ is the position vector of the *n*th expansion center, $\boldsymbol{r}$ is a vector pointing from this center to a point within cell n, and z is an (in general, complex) electron energy. The so-called single-site Green's function G^{ss} is

$$G^{ss}(\boldsymbol{r} + \boldsymbol{R}^n, \boldsymbol{r}' + \boldsymbol{R}^{n'}, z)$$
$$= 2m_e \delta_{nn'} \sum_{L=0}^{\infty} H_L^{n,\times}(\boldsymbol{r}_>, z) R_L^n(\boldsymbol{r}_<, z), \quad (4)$$

where $L = \{l, m\}$, i.e., the usual orbital angular momentum and magnetic quantum numbers, $H_L^n(\boldsymbol{r}, z)$ and $R_L^n(\boldsymbol{r}, z)$ are the irregular and the regular solutions of the Schrödinger equation, and $\boldsymbol{r}_>$ $(\boldsymbol{r}_<)$ means to take $\boldsymbol{r}$ or $\boldsymbol{r}'$ according to which one is greater (lesser) in magnitude. This single-site Green's function corresponds to the Green's function for a cell with free-electron boundary conditions. The so-called multisite Green's function is

$$G^{ms}(\boldsymbol{r} + \boldsymbol{R}^n, \boldsymbol{r}' + \boldsymbol{R}^{n'}, z)$$
$$= 2m_e \sum_{LL'}^{\infty} R_L^n(\boldsymbol{r}, z) \mathcal{G}_{LL'}^{nn'}(z) R_{L'}^{n'\times}(\boldsymbol{r}', z), \quad (5)$$

which can be viewed as a correction to the single-site Green's function that modifies the boundary conditions such that all incoming and outgoing waves from the cells match at the interfaces. The superscript $\times$ means to take the complex

conjugate of the angular part of H_L^n or R_L^n. Throughout, we use Hartree atomic units with $\hbar = 4\pi\epsilon_0 = e^2 = 1$, leaving m_e symbolic for easy conversion to Rydberg units. For other normalization and sign conventions, see Ref. [30].

The $\mathcal{G}_{LL'}^{nn'}(z)$ are elements of the so-called structural Green's function matrix $\boldsymbol{\mathcal{G}}(z)$. This is found by solving a variation of Dyson's equation, in what is sometimes referred to as the fundamental equation of MST,

$$\boldsymbol{\mathcal{G}}(z) = \boldsymbol{\mathcal{G}}_0(z)[I - \boldsymbol{t}(z)\boldsymbol{\mathcal{G}}_0(z)]^{-1}. \quad (6)$$

Here $\boldsymbol{t}(z)$ is the t matrix, found by matching the numerical solutions R_L^n and H_L^n to their free-electron forms at the cell boundaries [33]. In addition, $\boldsymbol{\mathcal{G}}_0(z)$ is the structure constant matrix. Its dependence on the set $\{\boldsymbol{R}_n\}$ has been suppressed in the notation. For a given set of expansion centers and energies, it can be calculated using a cluster approximation [31] or assuming a periodically repeating crystal structure [30]. Here we use the cluster approximation for all plasma conditions. For the initial state calculations for the Hugoniots (see Sec. III) we use the periodic crystal structure calculation.

In practice, these equations are solved using Mermin-Kohn-Sham density functional theory [34,35]. For a given set of expansion centers, the t-matrix, regular, and irregular solutions to the Kohn-Sham equation are found for all cells and the Green's function is then constructed. Note that the global t matrix $\boldsymbol{t}(z)$ is block diagonal. Each block element corresponds to a t matrix for a particular cell. In the calculations and results presented here we use the muffin-tin approximation, where the effective Kohn-Sham potential in each cell is spherically averaged inside the muffin-tin radius and takes a constant interstitial value elsewhere, as detailed in [30]. Further, we have used the temperature-dependent local density approximation (LDA) of Karasiev *et al.* [36] for the exchange and correlation functional. The nuclear positions are provided by an external model, pseudoatom molecular dynamics (PAMD) [37], which is thought to be accurate for all materials and conditions considered here. The equation of state is then calculated as a time average over uncorrelated time steps (Fig. 1).

The infinite sum over L in Eq. (4) is in practice converged automatically and only a finite number of terms are needed.[1] The two infinite sums in Eq. (5) are more challenging due to high computational expense. In practice, we use the method analyzed in Ref. [30], where only chemically relevant terms are retained. Here we keep terms up to and including $l = 2$, which should be sufficient for the cases considered here. Calculations with higher numbers of terms were considered in Ref. [30] but do not lead to significant changes to the EOS.

With the Green's function determined, the electron density is calculated

$$n_e(\boldsymbol{r}) = -\frac{2}{\pi} \Im \int_{-\infty}^{\infty} d\epsilon \, f(\epsilon, \mu) G(\boldsymbol{r}, \boldsymbol{r}, \epsilon), \quad (7)$$

where the 2 is due to spin degeneracy, the integral is along the real energy axis, and $f(\epsilon, \mu)$ is the Fermi-Dirac function with

---

[1]The number depends on the degeneracy of the system. For cold dense material, only a few terms are needed, while for hot dilute systems, many are needed.
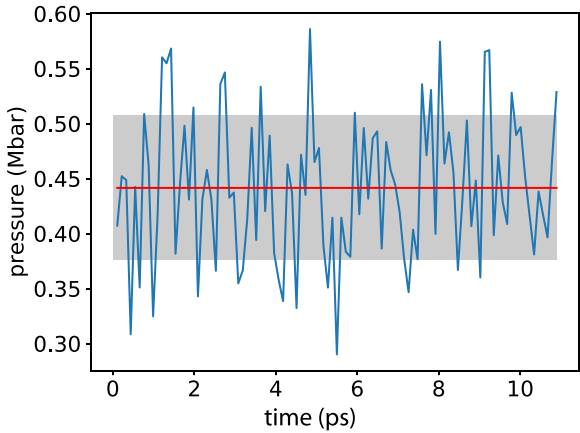
FIG. 1. Time variation of pressure for aluminum at 1 eV and 2.7 g/cm^3. The pressure fluctuates over molecular-dynamics time steps (blue line). The average pressure is shown by the red horizontal line and the gray area covers one standard deviation from this mean value. For this case, the time step is 2.2 fs and we calculate the pressure at every 50th time step.

chemical potential μ. A key advantage of the MST method is that, because the (retarded) Green's function is analytic in the upper-half complex energy plane, the energy integral in Eq. (7) can be carried out using Cauchy's integral theorem [38,39]. On the real energy axis, the full structure of the Green's function must be resolved. For periodic systems, this means that one would need to find all the discrete eigenvalues, a notoriously difficult problem [38]. By carrying out the inte-

gral in the complex energy plane, this problem is completely avoided: One no longer solves an eigenvalue problem. Moreover, the integrand becomes a smooth function of the energy away from the real energy axis [40], reducing the number of quadrature points needed.

The equations are then solved to self-consistency. We use Eyert's acceleration method, which is a quasi-Newton technique, to speed up convergence [41]. The equation of state can then be calculated using the method given in Ref. [30]. The initial guess for the potential in each cell is based on the Thomas-Fermi cell model [10].

III. RESULTS

As in Ref. [31], our physical model is a computational cube that is periodically repeated. As discussed above, a cluster approximation is used to solve Eq. (6). The cluster should contain enough centers in it such that adding more does not affect the desired quantities. Our cluster contains, at a minimum, the centers in the computational cube. We then add centers within a fixed distance, called the correlation radius, of any center in the computational cube. Hence, for zero correlation radius the cluster includes all centers within the computational volume, which for the cases presented here is 43 centers (8 nuclei plus 35 extra centers).

In Fig. 2 we show the effect of increasing cluster size on the pressure for density and temperature points close to the Hugoniot curve for aluminum. Figure 2 shows that for pressure, relative errors of less than 1% are achieved at 1 eV and 4.29 g/cm^3 with a correlation radius of 1.2 ion-sphere
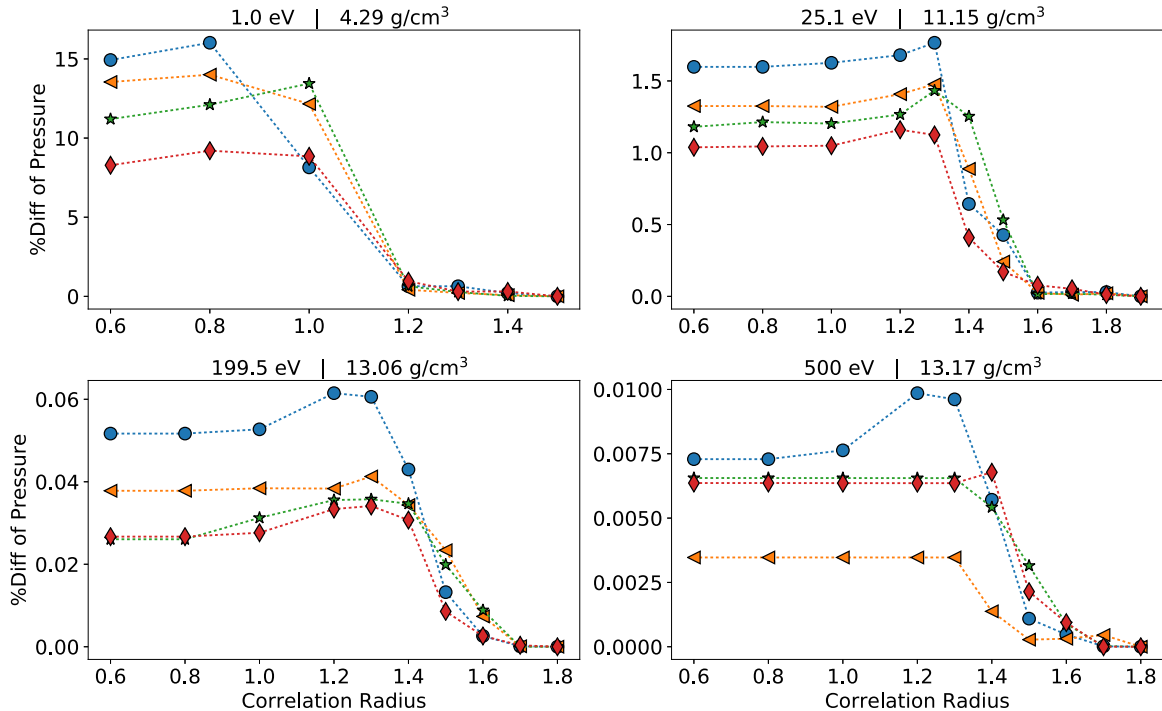

FIG. 2. Effect of the correlation radius on the pressure for aluminum plasmas at conditions close to points on the principal Hugoniot. Each panel corresponds to a different temperature and density. Each line corresponds to a different molecular-dynamics snapshot. The percent change in the pressure is relative to the value at the largest correlation radius shown. Note that the correlation radius is in units of ion-sphere radii for each case.

TABLE I. Effect of the number of extra centers on the pressure of carbon for a simulation with eight nuclei. No significant difference is observed at these conditions between 30 and 35 extra centers. We used 35 extra centers for all MD calculations presented, having checked convergence at other conditions.

Temperature	Density	Pressure (Mbar)		Absolute	Percent
(eV)	(g/cm^3)	8+30 centers	8+35 centers	difference	difference
10	3.52	10.205 ± 0.604	10.228 ± 0.627	0.0232	0.23%
100	3.52	140.038 ± 0.953	139.916 ± 1.084	0.1222	0.09%

radii, and for the highest-temperature case, much smaller relative errors are seen for all correlation radii. In between these extremes, the relative error steadily decreases as temperature increases. This behavior can be explained by noting that the relative contribution of the multiple scattering Green's function becomes smaller as temperature increases. This is because the scattering electrons have more energy on average and are therefore more free-electron-like. As such, the correction to the single-site term of the Green's function becomes smaller as temperature increases. This effect was already noted in Refs. [30,31]. The convergence of the internal energy is similar and is discussed in the Supplemental Material [42].

We have previously explored the effect that the number of extra expansion centers has on the EOS for aluminum plasmas (Ref. [31]). In Table I we show the effect of the number of extra centers on the pressure for carbon plasmas at two temperatures. Here we show the time-averaged pressure and standard deviation for a computational box with eight unique nuclei, for both 30 and 35 extra centers. For both temperatures the pressure is not significantly affected by the difference in the number of extra centers. For reference, we have used 8 nuclei, 35 extra centers, and 100 molecular-dynamics frames, for all plasma calculations presented here.

It is worth commenting on whether this number of particles is sufficient for the present purposes. Unfortunately, we cannot definitively answer this question quantitatively, as the memory requirement of our code currently limits calculations to these small systems. Based on other studies [43] and our own experience, we expect that larger system sizes will be necessary for more strongly correlated ionic fluids, i.e., lower temperatures and higher densities. For the principal Hugoniot, therefore, the points most affected will be those at low temperature, near the initial conditions. To mitigate this issue, we therefore only calculate Hugoniot points above 1 eV ($\approx 11\,600$ K).

The Hugoniot curve is the solution to the Rankine-Hugoniot equation

$$\tfrac{1}{2}(v_0 - v)(P + P_0) - (e - e_0) = 0, \tag{8}$$

where v is the specific volume, e the specific internal energy, and P the pressure. The subscript 0 refers to those quantities of the initial, unshocked, state of the material. Given an equation of state $P = P(v, T)$ and $e = e(v, T)$, Eq. (8) has a sequence of solutions (the Hugoniot) that can be expressed as $T(v)$. For an initial state, the resulting locus of final states in a single-shock experiment is the principal Hugoniot.

In Fig. 3 the principal Hugoniot for aluminum is shown. Let us first consider the full model calculation, labeled MST MD, which includes disordered, molecular-dynamics-determined, nuclear positions. The curve labeled MST fcc uses the same MST method but assumes an fcc crystal struc-

ture at all temperatures and densities. The initial state was calculated assuming an fcc structure for the structure constants and it is the same for both calculations. The differences between the calculations MST MD and MST fcc are then solely due to the treatment of the ionic disorder.

We see that overall, these calculations are in reasonable agreement, especially at high pressures, above 100 Mbar, corresponding to temperatures greater than 40 eV. This high-pressure region is where the ionization of the $n = 2$ (lower-pressure lobe) and $n = 1$ (higher-pressure lobe) shells occur. The reason that the ionic structure does not strongly influence these features is due to the increased thermal energy of the ionized electrons. They behave more free-electron-like and are therefore less sensitive to the ionic structure.

At lower pressures (12–100 Mbar) the calculation with ionic disorder (MST MD) predicts that the plasma is stiffer (less compressible) than the fcc calculation (MST fcc). In this pressure region, we find that both pressure and energy increase relative to the fcc calculation. At a given temperature, an increase in energy leads to a more compressible Hugoniot, while an increase in pressure leads to a stiffer, less compressible Hugoniot. Thus, the overall effect on the Hugoniot depends on a delicate interplay of these competing effects.
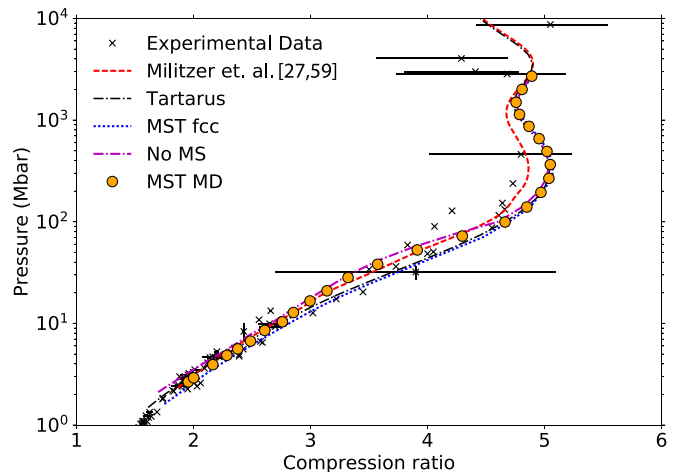

FIG. 3. Aluminum Hugoniot with experimental data [44–59]. Shown are results from the present model with molecular-dynamics configurations (MST MD), the present model with an fcc lattice (MST fcc), the Tartarus average atom model [15], and the FPEOS of Militzer and co-workers [27,60]. The "No MS" calculation is a simplified model described in the text. The two set of stars correspond to the temperatures labeled on the plot. Note that the initial density was taken to be 2.7 g/cm^3.

Also show in Fig. 3 is the result from the average atom model Tartarus [15], which does not include ionic disorder. From that point of view, it is even simpler than the MST fcc model, but is similar in spirit. The agreement between this model and the fcc calculation seems to bear this out. Some differences between these two models appear at low compressions and pressures. Clearly, the MST fcc calculation will give a much more realistic prediction of the initial state [61] than the average atom model, leading to the differences observed in the figure. Unfortunately, the experimental data, also shown in the figure, do not discriminate between the models. Modern shock experiments at very high pressure are starting to become available [3] and could potentially resolve some of the differences between models. Next we consider a simplified model, labeled "No MS" in Fig. 3. This model is identical to the full MST MD calculation except that we set the multiple scattering Green's function (5) to be identically zero. Thus, due to its relative computational simplicity and rapidity, it is a useful first approximation for including ionic structure and as such represents an intermediate model between an average atom and the full multiple scattering solution. Indeed, it agrees rather well with the full multiple scattering Hugoniot (Fig. 3), showing the stiffer feature for compressions of 2.5–4.5 that is seen in the full calculation. It does not agree perfectly, however, and in particular disagrees more for lower pressures (temperatures), where multiple scattering is more important.

Finally, we show comparison with the first-principles equation of state (FPEOS) calculation of Militzer and co-workers [27,60]. The FPEOS approach uses plane-wave-based DFT molecular-dynamics-based calculations up to 174 eV (∼700 Mbar) and then switches to path-integral Monte Carlo (PIMC) calculations for higher temperatures. There is good agreement between this method and MST MD for pressures below 70 Mbar and above 1 Gbar. In the region in between, corresponding to the ionization of the $n = 2$ shell, the FPEOS Hugoniot is significantly stiffer. This lobe on the Hugoniot is in the region covered by the DFT calculations in the FPEOS. Both our calculation and the FPEOS use eight-atom calculations in this region and both use an LDA for the exchange and correlation. We have used the temperature-dependent LDA of Karasiev et al. [36], whereas the FPEOS use the zero-temperature LDA of [62]. We have recalculated the Tartarus Hugoniot using a zero-temperature LDA [63] and found no significant difference (see [42]). Since the calculations both use DFT simulations of the same size and the difference is not due to the exchange and correlation functional, this leaves four possible sources for this discrepancy: (i) differences in the nuclear positions, (ii) some ill-converged numerical parameter, (iii) the muffin-tin approximation in MST, and (iv) the pseudopotential approximation in the FPEOS.

Let us address these in turn. (i) The good agreement of MST with the fcc calculation for the $n = 2$ feature strongly indicates that the ion positions should not be the source of the difference, provided reasonable MD configurations are used. (ii) We have checked that our calculation is converged in terms of the number of energy grid points, the correlation radius, the number of extra centers, and other internal numerical parameters. (iii) The muffin-tin approximation should perform more poorly at lower temperatures, where electrons have less
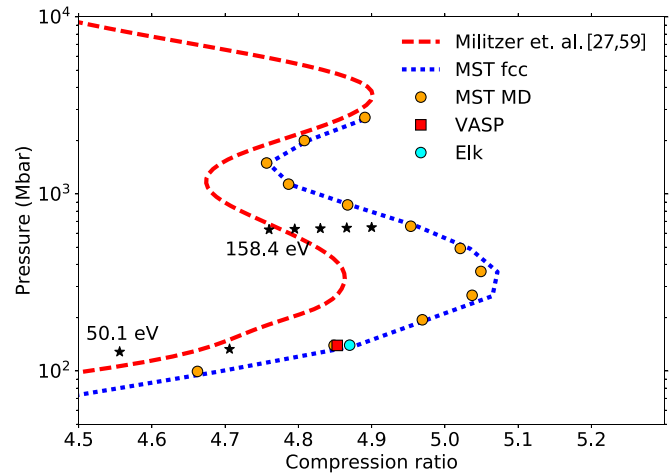

FIG. 4. Aluminum Hugoniot focused on the region of ionization of the $n = 2$ shell. Shown are results from the present multiple scattering calculation with an fcc lattice (MST fcc), the present model with molecular-dynamics configurations (MST MD), and the FPEOS of Militzer and co-workers [27,60]. The points labeled "Elk" and "VASP" are our own calculations of a Hugoniot point at 50.1 eV using the ELK [64] and VASP [65–67] codes, where an fcc lattice has been assumed. The black stars show the effect of reducing the MST internal energy in steps of $1E_H$ (right to left stars, starting at $1E_H$).

energy on average and are therefore more sensitive to the details of the potential. As the differences appear at rather high temperatures (greater than 40 eV), it is unlikely that the muffin-tin approximation is to blame. (iv) The pseudopotential approximation that appears in the plane-wave calculations does affect core states and has been the source of numerical issues in other calculations. The effect of the pseudopotential approximation on the EOS of aluminum has been quantified in Ref. [60], but we are unable to determine if the observed differences are sufficient to cause the discrepancies in the Hugoniot (Fig. 3).

The table in the Supplemental Material of Ref. [60] gives the EOS from which the Hugoniot curve was calculated therein. At a temperature of ∼174.2 eV and compression of 4.5, Ref. [60] reports energies and pressure from both calculation methods: PIMC and DFT MD. At that temperature [60] reported that DFT MD has an internal energy ∼5.3E_H lower than that for PIMC and a pressure ∼1% lower. We have checked the effects on the Hugoniot curve that such changes would have using our EOS. For pressure, a reduction of 1% moves the compression at 50.1 eV from 4.86 to 4.89 and at 158.4 eV from 4.94 to 4.97, i.e., relatively small effects. Figure 4 shows the effect of shifting the internal energy on the Hugoniot. At a temperature of 50.1 eV, a shift of just $1E_H$ is sufficient to explain the difference between MST and the FPEOS. At a temperature of 158.4 eV, the two calculations can be reconciled with a shift of 5E_H, which is comparable to the reported difference between PIMC and DFT MD at 174.2 eV. Further, also shown in Fig. 4 are our own calculations of Hugoniot points at 50.1 eV using the ELK code version 6.8.4 [64] and VASP version 5.4.4 [65–67]. Both calculations use an fcc crystal structure, adding on the ideal ion pressure and kinetic energy to determine the Hugoniot

point. In both codes, we use the LDA of Perdew and Zunger [63]. For ELK calculations, we constructed a species file that treats the $1s$ states as core states and the $2s$ and higher-energy states as valence states. This species file is constructed with a 0.6-bohr muffin-tin radius in order to ensure that nearest-neighbor atoms in the fcc configuration at the compressions studied do not overlap (the nearest-neighbor distance is roughly 3.2 bohrs at the levels of compression studied). In ELK, we use the built-in "very-high-quality" parameter set, with the exception that we further increase the default plane-wave cutoff energy to a value corresponding to 5442 eV. We also use a $12 \times 12 \times 12$ Γ-centered k-point grid (72 total irreducible k points) and 300 non-spin-polarized unoccupied states to ensure all states with fractional occupations of 10^{-10} and above are included in the calculation. Calculations are converged so that the total energy changes by less than 10^{-5} hartree and the Kohn-Sham potential changes by less than 10^{-6} hartree. For VASP calculations, we use the projector augmented wave (PAW) method [68] to treat the $1s$ core states, with the $2s$ and higher-energy states treated as valence states. The PAW potential we use was constructed specifically for LDA calculations, referred to as the `Al_sv_GW` PAW LDA potential in VASP [69]. This potential is constructed using a 1.7-bohr PAW radius, which at the compression studied in the fcc configuration allows the PAW radii of nearest neighbors to overlap by up to 7%. We also use a 3000-eV plane-wave energy cutoff and a $12 \times 12 \times 12$ Γ-centered k-point mesh (72 total irreducible k points) and include 200 non-spin-polarized bands to ensure inclusion of all states with fractional occupations of 10^{-6} and above. Calculations are converged so that the total energy changes to less than 10^{-6} eV. The Hugoniot points from both VASP and ELK agree well with our MST fcc calculation. In addition, we find that for fcc aluminum, the energies calculated using VASP, ELK, and MST along the 13.136-g/cm^3 isochore, from 1 eV up to 50.1 eV, are in excellent agreement (see the Supplemental Material [42]). Both the agreement in the Hugoniot points and the isochore provide strong verification of our code and method.

We have also performed MST calculations for carbon, assuming a diamond initial structure. The EOS of carbon is of interest due to its relevance to white dwarf modeling [3]. Figure 5 shows the principal Hugoniot for diamond. The crystal structure of diamond in the initial state presents a difficulty because, unlike an fcc structure, it is not closely packed. The expansion of the Green's function that only includes the nuclear centers is therefore inaccurate, in contrast to fcc structures. As a metric to appreciate this, the percentage of the volume in the muffin-tin spheres for fcc is 74% (using only nuclear positions as expansion centers). For diamond the number is 34%. Hence, we add eight extra expansion centers, filling 68% of the volume. This improves agreement of the MST result with our density of states calculations for diamond using ELK and VASP (Fig. 6). The remaining small differences are due to different broadening (0.5 eV for ELK and VASP versus 0.27 eV for MST) and the muffin-tin approximation.

The MST MD diamond Hugoniot agrees very well with the FPEOS calculation [78,79]. As for aluminum, the ionization feature due to the $1s$ shell is in good agreement between the approaches. The effect due to ionic disorder appears to be smaller than for aluminum, with a slight stiffening of the
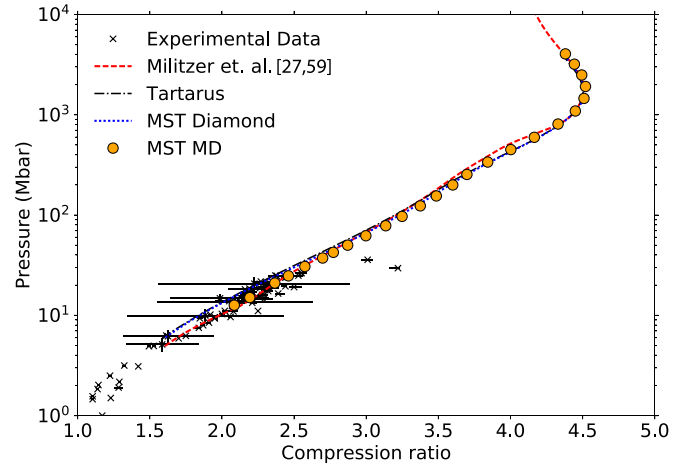

FIG. 5. Diamond Hugoniot with experimental data [70–77]. Shown are results from the present MST calculation with an assumed diamond structure (MST Diamond), the present model with molecular-dynamics configurations (MST MD), the FPEOS model [27], and the Tartarus average atom model [15]. Note that the initial density was taken to be 3.52 g/cm^3.

Hugoniot near a compression of 4. Differences between the full MST MD result and that assuming a diamond structure are largely confined to lower compressions. Note that the PAMD method for producing the nuclear positions is reliable for carbon only at elevated temperatures, roughly above 5 eV [80], due to a neglect of chemical bonds in that method. The first four points on our MST MD curve correspond to temperatures from 1.2 to 3.9 eV, while the fifth point is for a temperature of 6.3 eV. Hence, the nuclear positions are probably somewhat unrealistic for the first four points, where there is a small disagreement with the FPEOS results.

To explore further why the ionic structure seems to have more influence on the aluminum Hugoniot compared to that for carbon, in Fig. 7 we show the average ionization $\bar{Z}$ along these Hugoniots as predicted by the Tartarus average atom
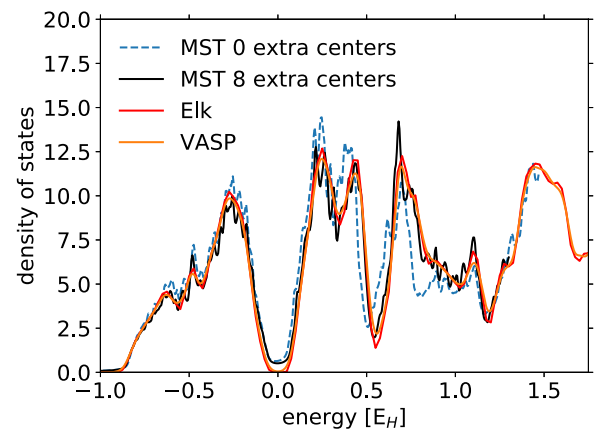

FIG. 6. Density of states for diamond at a temperature of 0.5 eV. The VASP and ELK calculations (present work) are compared to MST calculations. The MST calculation with eight extra expansion centers noticeably improves agreement with the VASP and ELK results, compared to the calculation with zero extra centers.
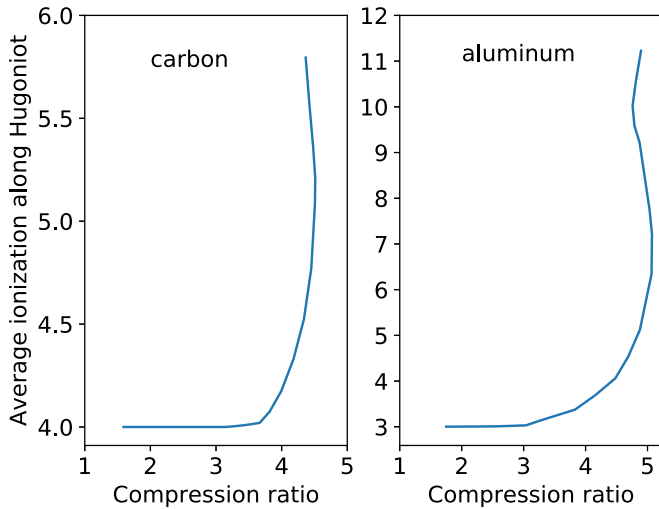
FIG. 7. Average ionization along principal Hugoniot from the Tartarus average atom model.

FIG. 8. Pressure along the 13.5-g/cm^3 isochore. Despite having relatively small influence on the Hugoniot curve, the effect of ionic disorder can be significant. Note that the vertical lines on the MST MD results show plus or minus one standard deviation (see Fig. 2).

model. As has been discussed many times, this quantity is not uniquely definable [15,81,82]. Here we choose to define ionized electrons as those having enough energy to escape the average atom potential. This includes, for example, electrons in resonance states, but not in bound states. This definition therefore is sensitive to changes in the states close to this threshold, which are also likely to be sensitive to the ionic environment. Figure 7 shows that for carbon, the $1s^2$ state does not start to ionize until the compression reaches ~3.6. This ionization corresponds to the slight stiffening of the Hugoniot near a compression of 4 mentioned above (Fig. 5). For aluminum $\bar{Z} \sim 3$ up to a compression of ~3, then ionization of the $n = 2$ shell begins. Again, this corresponds to the stiffening of the MST MD Hugoniot in Fig. 3. We therefore conclude that the Hugoniot is sensitive to ionic structure where shell ionization is beginning, for the two cases we have studied, and this effect is expected for other materials. In other words, the disordered ionic structure affects the ionization balance, and therefore the EOS, most strongly when states are close to the threshold. The size of the effect is larger for aluminum, presumably because the $n = 2$ shell contains eight electrons before it is ionized (out of a total of 13 per atom), whereas for carbon, the $n = 1$ shell contains only two out of six. The observed effects on the Hugoniots due to a disordered ionic environment are confined to this weakly-ionized-shell region and do not extend to higher pressures. This is due to the increased level of ionization being less sensitive to the ionic environment as these electrons are promoted into higher-lying energy states.

Finally, we note that, despite the relatively small influence of the ionic structure on the Hugoniot curve, the effect on an EOS point at a given temperature and density can be more impressive. This is shown in Fig. 8, where we compare the MST fcc and MD curves along the 13.5-g/cm^3 isochore for
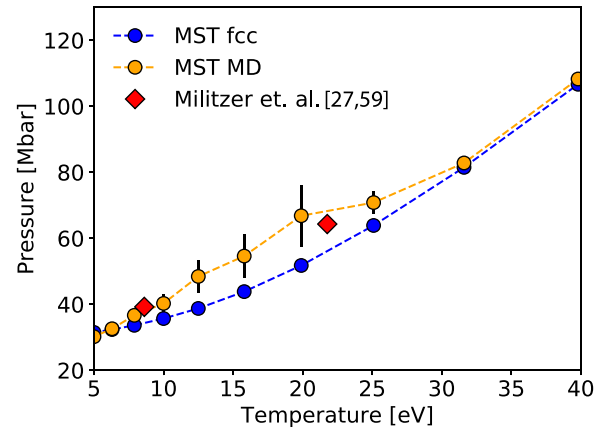
aluminum. The effect on pressure is large, with up to an ~30% increase over the fcc result observed.

IV. CONCLUSION

We have presented calculations of principal Hugoniots for diamond and aluminum using multiple scattering theory. Results including ionic disorder, through the use of molecular dynamics, as well as for fixed crystal structures, were given. It was found that ionic disorder has generally a small effect of the Hugoniot for the conditions considered and most strongly affects the Hugoniot curve where bound states are beginning to be ionized. For higher pressures (temperatures) still, the effect of ionic disorder is overwhelmed by the higher level of ionization and increased thermal energy of both the electrons and ions, which washes out the more subtle influence of the ionic disorder on the states near the ionization threshold. This result should give guidance to experimentalists seeking to understand comparisons of models with data. We also hope it will be useful to model developers in assessing the impact of ionic structure on shock Hugoniots.

Comparison was also made with the FPEOS model [27] and generally good agreement was found. The one instance of significant disagreement was the $n = 2$ shell ionization feature for aluminum. We have argued that this could be caused by the precision of the FPEOS results reported for that case.

[1] S. P. Marsh, *LASL Shock Hugoniot Data* (University of California Press, Berkeley, 1980), Vol. 5.

[2] J. D. Lindl, P. Amendt, R. L. Berger, S. G. Glendinning, S. H. Glenzer, S. W. Haan, R. L. Kauffman, O. L. Landen, and

L. J. Suter, The physics basis for ignition using indirect-drive targets on the national ignition facility, Phys. Plasmas **11**, 339 (2004).

[3] A. L. Kritcher, D. C. Swift, T. Döppner, B. Bachmann, L. X. Benedict, G. W. Collins, J. L. DuBois, F. Elsner, G. Fontaine, J. A. Gaffney *et al.*, A measurement of the equation of state of carbon envelopes of white dwarfs, Nature (London) **584**, 51 (2020).

[4] P. Dufour, J. Liebert, G. Fontaine, and N. Behara, White dwarf stars with carbon atmospheres, Nature (London) **450**, 522 (2007).

[5] W. J. Nellis, A. C. Mitchell, M. Van Thiel, G. J. Devine, R. J. Trainor, and N. Brown, Equation-of-state data for molecular hydrogen and deuterium at shock pressures in the range 2–76 GPa (20–760 kbar), J. Chem. Phys. **79**, 1480 (1983).

[6] H.-K. Mao and R. J. Hemley, Ultrahigh-pressure transitions in solid hydrogen, Rev. Mod. Phys. **66**, 671 (1994).

[7] R. Cauble, T. S. Perry, D. R. Bach, K. S. Budil, B. A. Hammel, G. W. Collins, D. M. Gold, J. Dunn, P. Celliers, L. B. Da Silva, M. E. Foord, R. J. Wallace, R. E. Stewart, and N. C. Woolsey, Absolute Equation-of-State Data in the 10–40 Mbar (1–4 TPa) Regime, Phys. Rev. Lett. **80**, 1248 (1998).

[8] T. Döppner, D. C. Swift, A. L. Kritcher, B. Bachmann, G. W. Collins, D. A. Chapman, J. Hawreliak, D. Kraus, J. Nilsen, S. Rothman, L. X. Benedict, E. Dewald, D. E. Fratanduono, J. A. Gaffney, S. H. Glenzer, S. Hamel, O. L. Landen, H. J. Lee, S. LePape, T. Ma *et al.*, Absolute Equation-of-State Measurement for Polystyrene from 25 to 60 Mbar Using a Spherically Converging Shock Wave, Phys. Rev. Lett. **121**, 025001 (2018).

[9] S. P. Lyon, SESAME: The Los Alamos National Laboratory equation of state database, Los Alamos National Laboratory Report No. LA-UR-92-3407, 1992 (unpublished).

[10] R. P. Feynman, N. Metropolis, and E. Teller, Equations of state of elements based on the generalized Fermi-Thomas theory, Phys. Rev. **75**, 1561 (1949).

[11] B. F. Rozsnyai, Relativistic Hartree-Fock-Slater calculations for arbitrary temperature and matter density, Phys. Rev. A **5**, 1137 (1972).

[12] R. Piron and T. Blenski, Variational-average-atom-in-quantum-plasmas (VAAQP) code and virial theorem: Equation-of-state and shock-Hugoniot calculations for warm dense Al, Fe, Cu, and Pb, Phys. Rev. E **83**, 026403 (2011).

[13] D. A. Liberman, Self-consistent field model for condensed matter, Phys. Rev. B **20**, 4981 (1979).

[14] B. Wilson, V. Sonnad, P. Sterne, and W. Isaacs, Purgatorio—A new implementation of the inferno algorithm, J. Quant. Spectrosc. Radiat. Transfer **99**, 658 (2006).

[15] C. E. Starrett, N. M. Gill, T. Sjostrom, and C. W. Greeff, Wide ranging equation of state with Tartarus: A hybrid Green's function/orbital based average atom code, Comput. Phys. Commun. **235**, 50 (2019).

[16] R. M. More, K. H. Warren, D. A. Young, and G. B. Zimmerman, A new quotidian equation of state (QEOS) for hot dense matter, Phys. Fluids **31**, 3059 (1988).

[17] J. D. Johnson, A generic model for the ionic contribution to the equation of state, High Press. Res. **6**, 277 (1991).

[18] S. C. Burnett, D. G. Sheppard, K. G. Honnell, and T. Sjostrom, in *Proceedings of the Conference of the American Physical Society Topical Group on Shock Compression of Condensed Matter, St. Louis, 2017*, edited by R. Chau, T. C. Germann, J. M. D. Lane, E. N. Brown, J. H. Eggert, and M. D. Knudson, AIP Conf. Proc. No. 1979 (AIP, Melville, 2018), p. 030001.

[19] L. Collins, I. Kwon, J. Kress, N. Troullier, and D. Lynch, Quantum molecular dynamics simulations of hot, dense hydrogen, Phys. Rev. E **52**, 6202 (1995).

[20] M. P. Desjarlais, Density-functional calculations of the liquid deuterium Hugoniot, reshock, and reverberation timing, Phys. Rev. B **68**, 064204 (2003).

[21] P. Suryanarayana, P. P. Pratapa, A. Sharma, and J. E. Pask, SQDFT: Spectral quadrature method for large-scale parallel $\mathcal{O}(N)$ Kohn–Sham calculations at high temperature, Comput. Phys. Commun. **224**, 288 (2018).

[22] S. Zhang, H. Wang, W. Kang, P. Zhang, and X. T. He, Extended application of Kohn-Sham first-principles molecular dynamics method with plane wave approximation at high energy—From cold materials to hot dense plasmas, Phys. Plasmas **23**, 042707 (2016).

[23] D. Sheppard, J. D. Kress, S. Crockett, L. A. Collins, and M. P. Desjarlais, Combining Kohn-Sham and orbital-free density-functional theory for Hugoniot calculations to extreme pressures, Phys. Rev. E **90**, 063314 (2014).

[24] A. Blanchet, M. Torrent, and J. Clerouin, Requirements for very high temperature Kohn–Sham DFT simulations and how to bypass them, Phys. Plasmas **27**, 122706 (2020).

[25] T. Sjostrom, S. Crockett, and S. Rudin, Multiphase aluminum equations of state via density functional theory, Phys. Rev. B **94**, 144101 (2016).

[26] A. J. White and L. A. Collins, Fast and Universal Kohn-Sham Density Functional Theory Algorithm for Warm Dense Matter to Hot Dense Plasma, Phys. Rev. Lett. **125**, 055002 (2020).

[27] B. Militzer, F. Gonzalez-Cataldo, S. Zhang, K. P. Driver, and F. Soubiran, First-principles equation of state database for warm dense matter computation, Phys. Rev. E **103**, 013203 (2021).

[28] J. Korringa, On the calculation of the energy of a Bloch wave in a metal, Physica **13**, 392 (1947).

[29] W. Kohn and N. Rostoker, Solution of the Schrödinger equation in periodic lattices with an application to metallic lithium, Phys. Rev. **94**, 1111 (1954).

[30] C. E. Starrett and N. Shaffer, Multiple scattering theory for dense plasmas, Phys. Rev. E **102**, 043211 (2020).

[31] M. Laraia, C. Hansen, N. R. Shaffer, D. Saumon, D. P. Kilcrease, and C. E. Starrett, Real-space Green's functions for warm dense matter, High Energy Density Phys. **40**, 100940 (2021).

[32] W. J. Herrera, H. Vinck-Posada, and S. G. Paez, Green's functions in quantum mechanics courses, arXiv:2107.14104.

[33] J. Zabloudil, R. Hammerling, L. Szunyogh, and P. Weinberger, *Electron Scattering in Solid Matter: A Theoretical and Computational Treatise* (Springer Science + Business Media, New York, 2006), Vol. 147.

[34] W. Kohn and L. J. Sham, Self-consistent equations including exchange and correlation effects, Phys. Rev. **140**, A1133 (1965).

[35] N. D. Mermin, Thermal properties of the inhomogeneous electron gas, Phys. Rev. **137**, A1441 (1965).

[36] V. V. Karasiev, T. Sjostrom, and S. B. Trickey, Finite-temperature orbital-free DFT molecular dynamics: Coupling profess and quantum espresso, Comput. Phys. Commun. **185**, 3240 (2014).

[37] C. E. Starrett, J. Daligault, and D. Saumon, Pseudoatom molecular dynamics, Phys. Rev. E **91**, 013104 (2015).

[38] H. Ebert, D. Koedderitzsch, and J. Minar, Calculating condensed matter properties using the KKR-Green's function method-recent developments and applications, Rep. Prog. Phys. **74**, 096501 (2011).

[39] P. Mavropoulos and N. Papanikolaou, in *Computational Nanoscience: Do It Yourself!*, edited by J. Grotendorst, S. Blügel, and D. Marx, Proceedings of the NIC Symposium 31 (John von Neumann Institute for Computing, Jülich, 2006), pp. 131-158.

[40] D. D. Johnson, F. J. Pinski, and G. M. Stocks, Fast method for calculating the self-consistent electronic structure of random alloys, Phys. Rev. B **30**, 5508 (1984).

[41] V. Eyert, A comparative study on methods for convergence acceleration of iterative vector sequences, J. Comput. Phys. **124**, 271 (1996).

[42] See Supplemental Material at http://link.aps.org/supplemental/10.1103/PhysRevE.104.055208 for details.

[43] J.-F. Danel and L. Kazandjian, Equation of state of a dense plasma by orbital-free and quantum molecular dynamics: Examination of two isothermal-isobaric mixing rules, Phys. Rev. E **91**, 013103 (2015).

[44] L. V. Al'tshuler and B. S. Chekin, All-Union Scientific-Research Institute of Physico-Technical and Radio Electronic Measurements report, 1974 (unpublished), p. 5.

[45] L. V. Al'tshuler and A. P. Petrunin, Rentgenographic investigation of compressibility of light substances under obstacle impact of shock waves, Zh. Tekh. Fiz. **31**, 717 (1961).

[46] L. V. Al'tshuler, N. N. Kalitkin, L. V. Kuz'mina, and B. S. Chekin, Shock adiabats for ultrahigh pressures, Zh. Eksp. Teor. Fiz. **72**, 317 (1977).

[47] E. N. Avronin, B. K. Vodolaga, N. P. Voloshin, V. F. Kuropatenko, G. V. Kovalenko, V. A. Simonenko, and B. T. Chernovolyuk, Pis'ma Zh. Eksp. Teor. Fiz. **43**, 309 (1986).

[48] V. A. Simonenko, N. P. Voloshin, A. S. Vladimirov, A. P. Nagibin, V. N. Nogin, V. A. Popov, and Y. A. Shoidin, Zh. Eksp. Teor. Fiz. **88**, 1452 (1985).

[49] B. L. Glushak, A. P. Zharkov, M. V. Zhernokletov, V. Y. Ternovoi, A. S. Filimonov, and V. E. Fortov, Sov. Phys. JETP **69**, 739 (1989).

[50] W. H. Isbell, F. H. Shipman, and A. H. Jones, General Motors Corp. Materials Science Laboratory Report No. MSL-68-13, 1968 (unpublished).

[51] S. B. Kormer, A. I. Funtikov, V. D. Urlin, and A. N. Kolesnikova, Dynamical compression of porous metals and the equation of state with variable specific heat at high temperatures, Zh. Eksp. Teor. Fiz. **42**, 686 (1962).

[52] R. G. McQueen, S. P. Marsh, J. W. Taylor, J. N. Fritz, and W. J. Carter, *High Velocity Impact Phenomena* (Academic, New York, 1970).

[53] A. C. Mitchell, W. J. Nellis, J. A. Moriarty, R. A. Heinle, N. C. Holmes, R. E. Tipton, and G. W. Repp, Equation of state of Al, Cu, Mo, and Pb at shock pressures up to 2.4 TPa (24 Mbar) J. Appl. Phys. **69**, 2981 (1991).

[54] R. F. Trunin, N. V. Panov, and A. B. Medvedev, Pis'ma Zh. Eksp. Teor. Fiz. **62**, 572 (1995).

[55] C. E. Ragan III, Shock compression measurements at 1 to 7 TPa, Phys. Rev. A **25**, 3360 (1982).

[56] C. E. Ragan III, Shock-wave experiments at threefold compression, Phys. Rev. A **29**, 1391 (1984).

[57] A. S. Vladimirov, N. P. Voloshin, V. N. Nogin, A. V. Petrovtsev, and V. A. Simonenko, Pis'ma Zh. Eksp. Teor. Fiz. **39**, 69 (1984).

[58] A. P. Volkov, N. P. Voloshin, A. S. Vladimirov, N. N. Nogin, and V. A. Simonenko, Pis'ma Zh. Eksp. Teor. Fiz. **31**, 623 (1980).

[59] I. S. Model', A. T. Narozhnyl, A. I. Kharchenko, S. A. Kholin, and V. V. Khrustalev, Pis'ma Zh. Eksp. Teor. Fiz. **41**, 6 (1985).

[60] K. P. Driver, F. Soubiran, and B. Militzer, Path integral Monte Carlo simulations of warm dense aluminum, Phys. Rev. E **97**, 063207 (2018).

[61] C. E. Starrett, High-temperature electronic structure with the Korringa-Kohn-Rostoker Green's function method, Phys. Rev. E **97**, 053205 (2018).

[62] D. M. Ceperley and B. J. Alder, Ground State of the Electron Gas by a Stochastic Method, Phys. Rev. Lett. **45**, 566 (1980).

[63] J. P. Perdew and A. Zunger, Self-interaction correction to density-functional approximations for many-electron systems, Phys. Rev. B **23**, 5048 (1981).

[64] The ELK code, http://elk.sourceforge.net/.

[65] G. Kresse and J. Hafner, *Ab initio* molecular dynamics for liquid metals, Phys. Rev. B **47**, 558 (1993).

[66] G. Kresse and J. Furthmüller, Efficient iterative schemes for *ab initio* total-energy calculations using a plane-wave basis set, Phys. Rev. B **54**, 11169 (1996).

[67] G. Kresse and J. Furthmüller, Efficiency of ab-initio total energy calculations for metals and semiconductors using a plane-wave basis set, Comput. Mater. Sci. **6**, 15 (1996).

[68] P. E. Blöchl, Projector augmented-wave method, Phys. Rev. B **50**, 17953 (1994).

[69] G. Kresse and D. Joubert, From ultrasoft pseudopotentials to the projector augmented-wave method, Phys. Rev. B **59**, 1758 (1999).

[70] H. Nagao, K. G. Nakamura, K. Kondo, N. Ozaki, K. Takamatsu, T. Ono, T. Shiota, D. Ichinose, K. A. Tanaka, K. Wakabayashi, K. Okada, M. Yoshida, M. Nakai, K. Nagai, K. Shigemori, T. Sakaiya, and K. Otani, Hugoniot measurement of diamond under laser shock compression up to 2 TPa, Phys. Plasmas **13**, 052705 (2006).

[71] M. N. Pavlovskii, Shock compression of diamond, Fiz. Tverd. Tela **13**, 893 (1971).

[72] K.-i. Kondo and T. J. Ahrens, Shock compression of diamond crystal, Geophys. Res. Lett. **10**, 281 (1983).

[73] M. C. Gregor, D. E. Fratanduono, C. A. McCoy, A. Sorce, D. N. Polsin, J. R. Rygg, G. W. Collins, T. Braun, P. M. Celliers, J. H. Eggert, D. D. Meyerhofer, and T. R. Boehly, Hugoniot and release measurements in diamond shocked up to 26 Mbar, Phys. Rev. B **95**, 144114 (2017).

[74] M. Millot, P. A. Sterne, J. H. Eggert, S. Hamel, M. C. Marshall, and P. M. Cellier, High-precision shock equation of state measurements for metallic fluid carbon between 15 and 20 Mbar, Phys. Plasmas **27**, 102711 (2020).

[75] K. Katagiri, N. Ozaki, Y. Umeda, T. Irifune, N. Kamimura, K. Miyanishi, T. Sano, T. Sekine, and R. Kodama, Shock Response of Full Density Nonopolycrystalline Diamond, Phys. Rev. Lett. **125**, 185701 (2020).

[76] R. S. McWilliams, J. H. Eggert, D. G. Hicks, D. K. Bradley, P. M. Celliers, D. K. Spaulding, T. R. Boehly, G. W. Collins,

and R. Jeanlo, Strength effects in diamond under shock compression from 0.1 to 1 TPa, Phys. Rev. B **81**, 014111 (2010).

[77] A. V. Bushman, I. V. Lomonosov, K. V. Khishchenko, V. P. Kopyshev, E. A. Kuzmenkov, V. E. Kogan, P. R. Levashov, and I. N. Lomov, Shock wave database (unpublished).

[78] K. P. Driver and B. Militzer, All-Electron Path Integral Monte Carlo Simulations of Warm Dense Matter: Application to Water and Carbon Plasmas, Phys. Rev. Lett **108**, 115502 (2012).

[79] L. X. Benedict, K. P. Driver, S. Hamel, B. Militzer, T. Qi, A. A. Correa, A. Saul, and E. Schwegler, Multiphase equation of state

for carbon addressing high pressures and temperatures, Phys. Rev. B **89**, 224109 (2014).

[80] C. E. Starrett, D. Saumon, J. Daligault, and S. Hamel, Integral equation model for warm and hot dense mixtures, Phys. Rev. E **90**, 033110 (2014).

[81] P. A. Sterne, S. B. Hansen, B. G. Wilson, and W. A. Isaacs, Equation of state, occupation probabilities and conductivities in the average atom Purgatorio code, High Energy Density Phys. **3**, 278 (2007).

[82] M. S. Murillo, J. Weisheit, S. B. Hansen, and M. W. C. Dharma-wardana, Partial ionization in dense plasmas: Comparisons among average-atom density functional models, Phys. Rev. E **87**, 063113 (2013).